PCCP

PAPER

View Article Online
View Journal | View Issue

Cite this: *Phys. Chem. Chem. Phys.*, 2019, **21**, 16718

Defect tolerant and dimension dependent ferromagnetism in $MnSe_2$†

I. Eren,[a] F. Iyikanat [a] and H. Sahin *[bc]

Received 1st June 2019,
Accepted 12th July 2019

DOI: 10.1039/c9cp03112j

rsc.li/pccp

By performing density functional theory-based calculations, we investigate the structural, vibrational, electronic and magnetic properties of 2D monolayers, nanoribbons and quantum dots of $MnSe_2$. Vibrational spectrum analysis reveals the dynamical stability of not only ferromagnetic but also antiferromagnetic phases of single layer $MnSe_2$ crystal structures. Electronically, calculations show that 1T-$MnSe_2$ is a ferromagnetic structure displaying metallic behavior. It is also found that the structure preserves its dynamical stability and metallic behavior even under the presence of high density Se vacancies. Moreover, it was predicted that, differing from the 2D $MnSe_2$, metal–metal interaction driven reconstructions result in ferromagnetic-to-antiferromagnetic crossover in the ground state of nanoribbons and quantum dots. With its robust ferromagnetic metallic character in the 2D ultra-thin limit and dimension-dependent magnetic properties, $MnSe_2$ is an important candidate for spintronic device applications.

1 Introduction

The successful synthesis of graphene has transformed two-dimensional (2D) layered materials into a highly studied material group in the last decade.[1,2] Besides graphene, other 2D materials such as hexagonal boron nitride (h-BN),[3–5] silicene,[6–8] borophene,[9–11] black phosphorus,[12–14] and transition metal dichalcogenides (TMDs),[15–21] have gained much attention owing to their wide range of electronic and optical properties. Among the ultra-thin materials, transition metal dichalcogenides have been promising candidates for nanoelectronic device applications with their unexpected properties in bulk and monolayer forms.

Depending on the atomic type and arrangement of the atoms, TMDs can display metallic,[22] semimetallic[23] or semiconducting behavior.[24] Recent experimental studies showed that as the number of layers decreases from bulk to monolayer, indirect-to-direct band gap crossover occurs in semiconducting TMDs.[25–27] Thanks to their direct band gap, monolayer TMDs are quite suitable materials for optoelectronic applications and field-effect transistors. Recently, field effect transistors based on monolayer MoS_2 have been fabricated, demonstrating a room-temperature carrier mobility over 200 cm^2 $(V\ s)^{-1}$.[28] Moreover, it was shown that monolayer MoS_2 and WSe_2 exhibit high photoluminescence (PL) quantum yield.[24,29] Although electronic and optical properties of TMDs have been studied extensively, investigation of the magnetic properties of TMDs are still limited.

Magnetism in 2D materials has recently attracted significant attention with the discovery of long-range intrinsic magnetic order in ultra-thin materials which has various applications in sensing and data storage.[30,31] It was found that single-layer transition metal halides exhibit intrinsic magnetism with strong magnetic anisotropy.[32–35] Moreover, it was revealed that the magnetization of the CrI_3 directly depends on the number of layers.[36] In addition, intrinsic long-range ferromagnetic order is revealed in $Cr_2Ge_2Te_6$.[37] Recent studies have shown that some TMDs exhibit intrinsic magnetism at the ground state. Among them 1T-$FeCl_2$ is a half-metallic material with intrinsic ferromagnetic ground state.[38] More recently, Bonilla *et al.* synthesized a monolayer VSe_2, which is intrinsic ferromagnet at room temperature while its bulk phase is paramagnetic.[39] VSe_2 possesses 1T and 2H phases and it is metallic in the former phase, while it is semiconductor in the latter phase. Additionally, room temperature ferromagnetism has been observed in the recently synthesized epitaxial manganese selenide films grown by MBE.[40] They provided strong evidence that ferromagnetism in monolayer $MnSe_x$ originates from 1T-$MnSe_2$ monolayer.

Motivated by these studies, in this paper, we investigated (i) structural, vibrational, electronic and magnetic properties of single-layer $MnSe_2$, (ii) formation of Se vacancy in the material and its influence on the vibrational, electronic and magnetic properties, and (iii) effect of dimensional reduction on the electronic and magnetic properties of the material. The paper is organized as follows: details of the computational methodology are given in the Section 2. Structural, vibrational, electronic and

[a] *Department of Physics, Izmir Institute of Technology, 35430, Izmir, Turkey*
[b] *Department of Photonics, Izmir Institute of Technology, 35430, Izmir, Turkey. E-mail: hasansahin@iyte.edu.tr*
[c] *ICTP-ECAR Eurasian Center for Advanced Research, Izmir Institute of Technology, 35430, Izmir, Turkey*

† Electronic supplementary information (ESI) available. See DOI: 10.1039/c9cp03112j

magnetic properties of the pristine and vacancy defected single-layer $MnSe_2$ are presented in Section 3. The effect of dimensional reduction on the characteristic properties of $MnSe_2$ are debated in Sections 4 and 5. Lastly, results are concluded in Section 6.

2 Computational methodology

For structural optimizations and determination of electronic and magnetic configurations of single-layer $MnSe_2$, we carried out first-principles calculations within density functional theory (DFT) using the plane-wave projector-augmented wave (PAW) method[41] implemented in the Vienna *ab initio* Simulation Package (VASP).[42,43] For the exchange–correlation energy, the Perdew–Burke–Ernzerhof form of the generalized gradient approximation (GGA) was used.[44] DFT+U method described by Dudarev was also used to take into account strong correlations between d-orbitals of Mn atoms.[45] In accordance with the previous study, the effective U parameter was chosen to be U_{eff} = 3.9 eV.[46]

The conjugate gradient algorithm was used to optimize all the structures. The kinetic energy cutoff of the plane-wave basis set was 500 eV in all calculations. The van der Waals corrections were implemented by the DFT-D2 method of Grimme.[47] The total energy difference between the sequential steps in the iterations was taken as 10^{-5} eV as convergence criterion. The convergence criterion for the Hellmann–Feynman forces was taken to be 10^{-4} eV Å^{-1}. The Gaussian broadening for the density of states calculation was taken to be 0.05. The pressures on the unit cell were reduced to a value of less than $1k_B$ in all directions. In order to hinder interactions between the adjacent cells, at least 10 Å vacuum spacing was used along the z-direction. Γ-Centered k-point mesh was used with grid sizes of 36 × 36 × 1 for the density of states (DOS) calculations of the unit cell. The k-point mesh was scaled according to the size of supercells. Phonon calculations were performed by making use of the small displacement method as implemented in the PHONOPY code.[48] Analysis of the charge transfers in the structures was determined by the Bader technique.[49]

3 Characteristic properties and defect tolerance of 2D $MnSe_2$

Monolayer $MnSe_2$ consists of stacked Se–Mn–Se atomic layers. We carefully optimized the atomic structure of the monolayer $MnSe_2$ starting from the experimentally observed lattice parameter.[40] Our calculations show that the lattice parameter of the ferromagnetic (FM) phase is 3.59 Å which is in good agreement with the previous theoretical prediction.[50] To examine the magnetic coupling between Mn atoms a (2 × 2) supercell is constructed with FM and antiferromagnetic (AFM) initial magnetic configurations. The optimized atomic structures and spin-polarized charge densities of (2 × 2) FM and (2 × 2) AFM phases of monolayer $MnSe_2$ are shown Fig. 1. It is found that while the monolayer $MnSe_2$ displays FM behavior with 3.05 μ_B per unit cell in its ground state, AFM order has 57 meV less favorable energy per formula. Each Mn atom in both magnetic phases has a magnetic moment of ~3.9 μ_B consistent with the experimental results.[40]

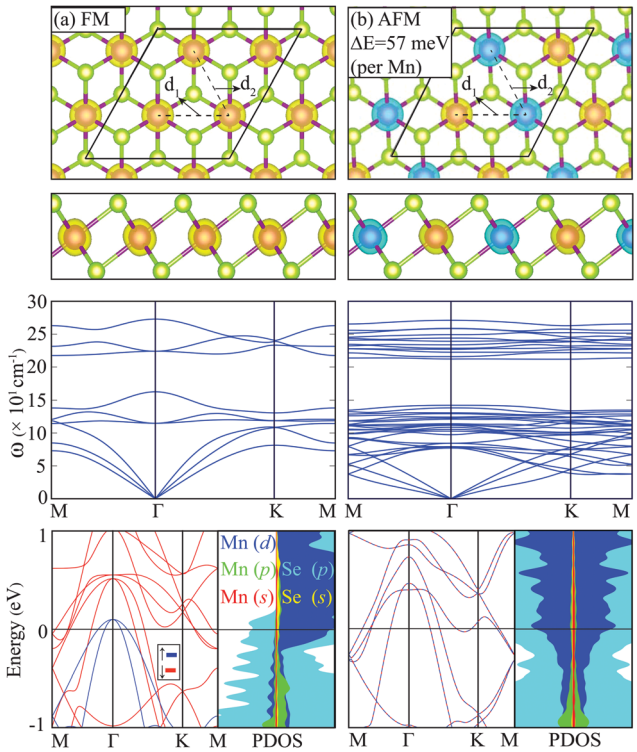

Fig. 1 Top and side views of the spin density plots (isosurface value of 0.06 e Å^{-3}), phonon-band structures, electronic band dispersions and partial density of states of (a) FM and (b) AFM configurations of monolayer $MnSe_2$. Yellow and blue isosurfaces represent majority and minority spin densities, respectively.

Table 1 Calculated parameters for the FM and AFM configurations of monolayer 1T-$MnSe_2$; (2 × 2) supercell lattice constant, a; Mn–Se distances, d_1 and d_2; thickness, h; magnetic moment per (2 × 2) supercell, μ; the cohesive energy per formula, E_{Coh}; the charge transfer between atoms, $\Delta\rho$; the ground state energy difference per Mn atom, ΔE

	a (Å)	d_1 (Å)	d_2 (Å)	h (Å)	μ (μ_B)	E_{Coh} (eV)	$\Delta\rho$ (e)	ΔE (eV)
FM	7.17	3.59	3.59	2.96	12.2	9.55	0.5	—
AFM	6.95	3.48	3.57	3.11	0.0	9.49	0.5	0.057

Octahedron distances (d_1 and d_2) and lattice parameters of (2 × 2) FM and (2 × 2) AFM phases are given in Table 1. It is seen that the FM order exhibits a perfect 1T phase, and thus d_1 and d_2 are the same and equal to 3.59 Å. However, magnetic interactions between Mn atoms of the AFM phase lead to dimer formation by reducing the d_1 and d_2 to 3.48 and 3.57 Å, respectively. Therefore, different magnetic orders among Mn atoms cause the monolayer to have different lattice parameters in FM and AFM phases. While the bond distance between Mn and Se atoms for FM state is 2.55 Å, that of AFM state vary from 2.55 to 2.56 Å. To obtain the partial charge on the atoms, the Bader technique was performed. In the Bader charge analysis, atoms are defined by volumes bounded by surfaces of the zero-flux. The integrated charges in the volume attributed to atoms

are defined as Bader charge. According to the Bader analysis, charge donation from Mn to Se atoms is 0.5 e in both magnetic states.

For examination of the dynamical stabilities of both phases, phonon calculations are also performed. As shown in Fig. 1(a and b), in the whole Brillouin zone of the crystal structure phonon modes have positive eigenfrequencies and therefore both FM and AFM states are dynamically stable. This is in agreement with the experimental result of O'Hara *et al.*[40] reporting the stability of FM state. The FM phase of monolayer $MnSe_2$ has 9 phonon branches, 3 acoustic and 6 optical. However, due to the larger unit cell, phonon dispersion of the AFM phase of monolayer $MnSe_2$ yields 3 acoustic and 33 optical branches. Vibrational properties of the magnetic states show similarity at the top phonon branches. The phonon band with highest energy at 272.9 cm^{-1} for FM state, and 271.1 cm^{-1} for AFM state. Not only the highest phonon frequency of both magnetic states are similar to each other but also phonon band gaps are similar and which are 61.3 cm^{-1} for the FM state and 69.9 cm^{-1} for the AFM state. Frequencies of acoustic phonon modes of the FM state are above 70.0 cm^{-1} at the M point. In the AFM state, two acoustic phonon modes are around 50.0 cm^{-1} at the M point indicating that magnetic state transition from FM to AFM leads to phonon softening at the acoustic phonon modes in the monolayer.

The spin-resolved band structure of FM and AFM configurations of monolayer $MnSe_2$ based on GGA are shown in the bottom panels of Fig. 1(a and b), respectively. Since the octahedral 1T-$MnSe_2$ exhibits inversion symmetry and does not contain heavy atoms, spin orbit coupling (SOC) has a negligible effect on the electronic structure of the material. Therefore, the SOC effect is not taken into account in our calculations. In accordance with previous studies, our calculations show that both FM and AFM phases are metallic.[51,52] While the valence and conduction bands of the former has a large spin splitting, that of the latter consist of degenerate spin up and spin down states. In a previous study, monolayer $MnSe_2$ is found to be a semiconductor with a very small band gap of 10 meV with HSE06 functional.[50] However, it was reported earlier that the ground state electronic and magnetic properties of metallic systems are incorrectly calculated with hybrid functionals.[53–55] Therefore, we prefer to use the DFT+U method in all calculations throughout this study.

Partial density of states (PDOS) calculations show that the states in the vicinity of the Fermi level are mostly dominated by Mn-d and Se-p orbitals. Overlap between the d orbitals of metal atom and p orbitals of chalcogen atom around the Fermi level is a characteristic of lamellar TMD crystals.[56]

Moreover, the Curie temperature of the monolayer $MnSe_2$ is also calculated. The Curie temperature of a material can be approximated using the Heisenberg model in which the Hamiltonian is described by

$$H = -J \sum_{i,j} \hat{m}_i \hat{m}_j \quad (1)$$

where J is the Heisenberg exchange parameter, $\hat{m}$ is the magnetic moment (μ_B) of each site. Only the nearest neighbor exchange interaction is taken into account. Therefore, the expression for the J parameter for our system is $J = E_{exc}/12m^2$, where E_{exc} ($= E_{AFM} - E_{FM}$) is the exchange energy per conventional cell. Our calculations show that E_{exc} and J are 229 and 2.051 meV, respectively. Using the mean field approximation, which is $k_B T_c = 3/2J$, the Curie temperature, T_c, is found to be 35.7 K.

Whether it is chemically grown or exfoliated from bulk, formation of chalcogen defects during the experimental synthesis procedure of TMDs is inevitable.[57,58] Therefore, investigation the effect of such point defects on the electronic, magnetic and vibrational characteristics of the monolayer $MnSe_2$ is of importance. To avoid the defect–defect interaction between neighboring cells Se vacancy is created in a large $5 \times 5 \times 1$ supercell. Optimized atomic structures and spin polarized charge densities of Se defected $MnSe_2$ with two different magnetic configurations are shown in the Fig. 2(a). Differing from the pristine structure, the energetically second favorable magnetic structure, AFM′, is formed when the three Mn atoms closest to the Se defect have the opposite spin orientation to the other Mn atoms. Considering the total energies for two defected magnetic phases, FM state is still (15 meV per formula) favorable over the AFM′ state. After the defect formation net magnetic moment of the FM state is slightly increased to 3.12 μ_B, while that of AFM′ state remains the same.

Furthermore, phonon dispersions shown in Fig. 2 reveal that both FM and AFM′ states are dynamically stable even after the defect formation. It is seen that compared to their defect-free structures the presence of defects leads to phonon softening in both FM and AFM′ phases. While general phonon dispersion stays unchanged after defect formation, three dispersionless phonon branches appear at 174–184 cm^{-1}. As shown in Fig. 2, these states correspond to local vibrations of atoms surrounding the defective region. Presence of such distinctive phonon modes provides an easy tool for defect detection in $MnSe_2$ *via* Raman spectrum measurements.

4 1D nanoribbons of $MnSe_2$

Synthesis of 1D ribbon forms of 2D crystals not only results in dimensional reduction but also lead to emergence of novel functionalities in the structure. It has been shown that nanoribbons of graphene and MoS_2 exhibit suitable and tunable bandgap which makes these materials important candidates for optoelectronic applications.[59–61] In this section, structural, electronic and magnetic properties of 1D nanoribbons of $MnSe_2$ are investigated.

Similar to graphene and TMDs such as MoS_2, it can be assumed that the formation of nanoribbons of 1T-$MnSe_2$ single layers can occur in two main crystallographic directions; zigzag (ZZ) and armchair (ARM). For the ARM nanoribbons, the edges are terminated by Mn and Se atoms. For the ZZ nanoribbons, since the Se-edged nanoribbons exhibit a rather complex edge reconstructions only the structures whose edges are terminated with Mn atoms are considered. As seen in the inset of Fig. 3(b), the width of the nanoribbon is defined according to the number of Mn atoms (n-ARM and n-ZZ) across the ribbon

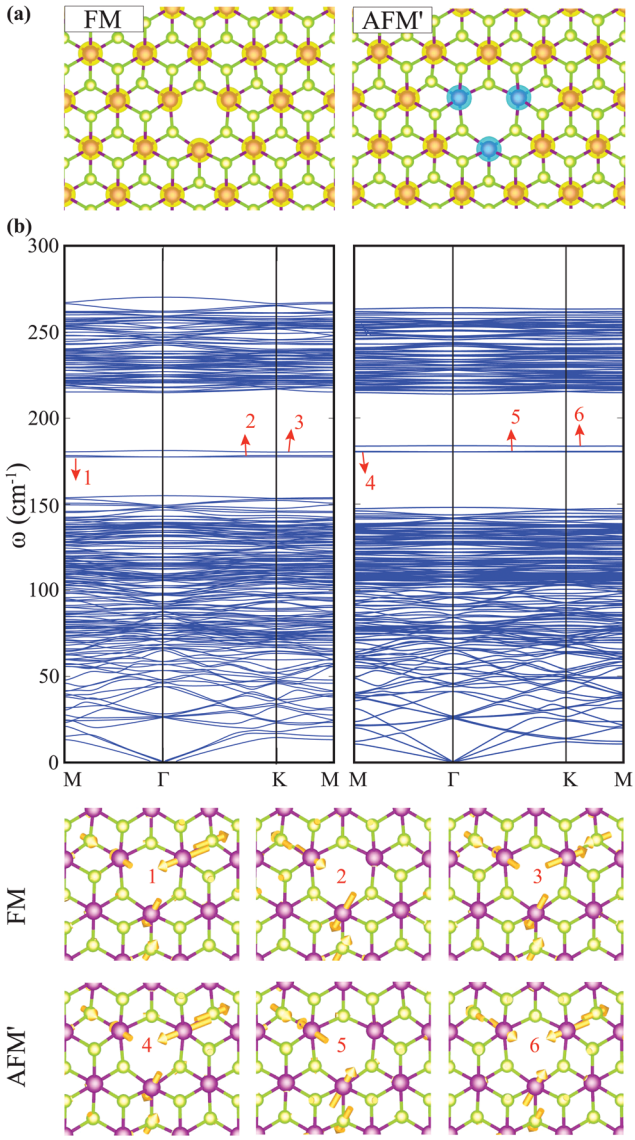

Fig. 2 Top views of the spin density plots (isosurface value of 0.06 e Å^{-3}) and phonon band structures of (left) FM and (right) AFM′ states of defected monolayer $MnSe_2$. Atomic motions around the defect are depicted for the FM and AFM′ phases. Yellow and blue isosurfaces represent majority and minority spin densities, respectively.

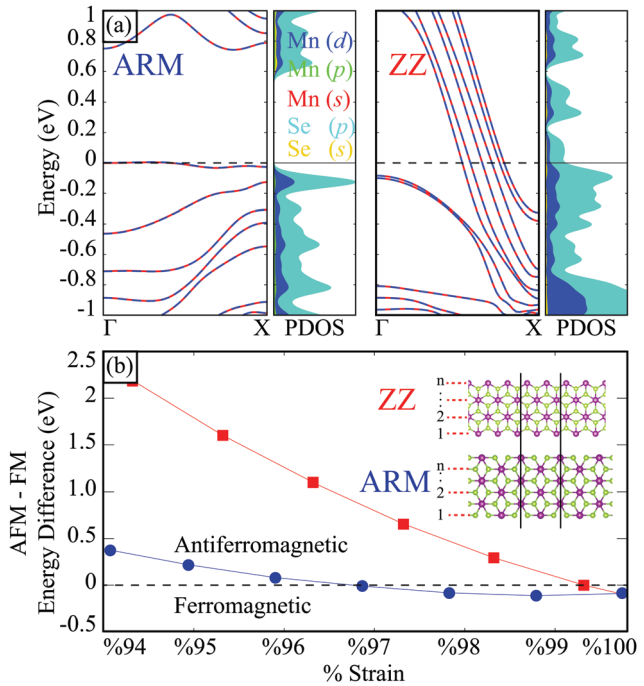

Fig. 3 (a) Electronic band dispersions of 3-ARM (blue) (top left) and 4-ZZ (red) (top right) nanoribbons of $MnSe_2$. (b) Strain dependent energy difference comparison between FM and AFM magnetic states of 3-ARM (blue) and 4-ZZ (red) nanoribbons of $MnSe_2$. Initial atomic configurations of ARM and ZZ ribbons are shown in the inset. The black lines show the unitcell of the corresponding ribbon.

width. The optimized geometric structures and spin polarized charge densities of ZZ and ARM nanoribbons for different ribbon widths are shown in Fig. S1 (ESI†). It is seen that the presence of edge states causes significant reconstructions on the edge and middle regions. For a reliable simulation of the possible edge reconstructions and antiferromagnetic orderings multiple unit cells are used along the axis of the nanoribbons. Electronic and magnetic properties of 4-ZZ and 3-ARM are investigated in detail. Calculated minimum and maximum bond lengths for 4-ZZ (3-ARM) nanoribbons are 2.49 and 2.85 Å (2.48 and 3.03 Å), respectively. As shown in Fig. 3(a), 3-ARM displays semiconducting behavior while 4-ZZ exhibits metallic character. Moreover, ribbon-width dependent electronic structures of ZZ and ARM nanoribbons are also investigated. Fig. S1 (ESI†) shows that regardless of thickness, ZZ and ARM ribbons retain their metallic and semiconductor properties respectively. It is also seen from the atom-projected density of states calculations that flat bands of ARM nanoribbons and highly dispersive bands of ZZ nanoribbons at the vicinity of the Fermi level are composed of Mn-d and Se-p orbitals. In addition, our analysis on the magnetic ground state of nanoribbons reveals that reconstruction-driven shrinkage in the lattice parameter also results in FM to AFM transition. Fig. 3(b) shows that AFM state becomes more favorable for ARM (ZZ) nanoribbons starting from 3% (0.5%) contraction in the lattice.

Briefly, the ZZ and ARM nanoribbons are both in the AFM ground state and differ from 2D counterpart. However, while the ZZ structure continues to protect its electronic configuration as metal, the ARM nanoribbons become semiconductor.

5 0D quantum dots of $MnSe_2$

Experiments have revealed that during the chemical growth and mechanical exfoliation of TMDs mostly triangle shaped flakes are formed.[62–64] Therefore, in order to see how characteristic properties of single layer $MnSe_2$ are modified by its dimension, investigation of triangular flakes (TFs) is essential. As shown in Fig. 4(a), depending on whether the edge is terminated by Mn or Se atoms, $MnSe_2$ TFs undergo different type of structural modifications. The triangular quantum dots examined in this study are denoted as xTF, where x is the number of edge atoms.

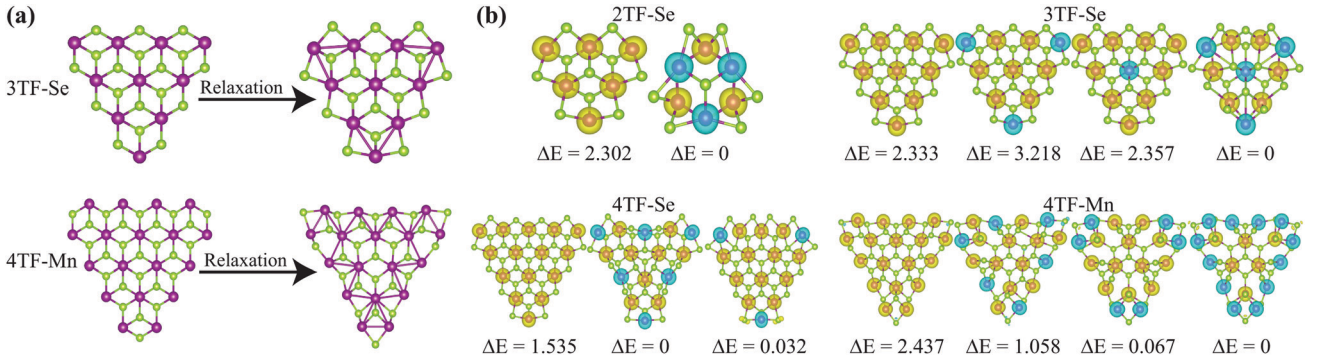

Fig. 4 (a) Geometric configurations of triangular flakes (TFs) of $MnSe_2$ before and after geometric optimization. (b) Spin polarized charge density distributions of various magnetic phases of TFs of $MnSe_2$. The total energy differences (in eV) of each TF with respect to the magnetic ground state are also shown.

Structural relaxations of Se-terminated TFs (TF-Se) show that despite the local relaxations induced by metal–metal bonds at the corners there is no noticeable modification in the atomic arrangement. On the other hand, for Mn-edged TFs (TF-Mn), $MnSe_6$ octahedra at the edges are highly distorted *via* formation of Mn–Mn dimers. Such reconstructions have also been reported before for other single layer TMDs such as ReS_2, $MoTe_2$ and WTe_2.[65–67]

Magnetic characteristics of 2TF, 3TF, and 4TF quantum dots of $MnSe_2$ are also investigated *via* spin polarized charge densities. As shown in Fig. 4(b), in addition to their FM state each TF can have various AFM orderings. Here, it is also worth to note that due to the strong magnetic interactions each AFM state that is considered corresponds to a different atomic structure. Total energy calculations reveal that the reconstruction of the edge atoms of structurally optimized TFs caused the quantum dots to have much lower energy than the non-optimized (static) state. While the magnetic moment per Mn atom of 2TF, 3TF, and 4TF is in the range of 4–4.5 μ_B, the spin polarized charge densities are almost evenly distributed throughout the flakes. It is seen that spin polarized charge densities of 2TF, 3TF, and 4TF are almost evenly distributed throughout the flakes. The magnetic ground state analysis reveals that the AFM configuration of all the TFs is more favorable than the FM configuration. In addition, size dependent total energy differences per Mn atom of AFM and FM Se-edged TFs are also calculated and it is found that as the size of the TFs increases, the total energy differences decreases, as expected. (the energy differences are 0.384 eV, 0.233 eV and 0.102 eV for 2TF-Se, 3TF-Se and 4TF-Se, respectively) Moreover, it is seen that both AFM and FM configurations of Mn-edged TFs show highly distorted $MnSe_6$ octahedra at the edges. On the other hand, the FM configurations of Se-edged TFs tend to maintain form of $MnSe_6$ octahedra at the edges, while that of some AFM configurations exhibit significant reconstructions.

6 Conclusions

To sum up, we utilized first-principles calculations with density functional theory to investigate the structural, vibrational, electronic and magnetic features of 2D single layers, nanoribbons and quantum dots of $MnSe_2$. Vibrational analysis confirmed that both FM and AFM phases of monolayer $MnSe_2$ are dynamically stable, while energetically the magnetic ground state of metallic monolayer $MnSe_2$ is FM. It was also found that despite the presence of high density Se vacancies the single layer $MnSe_2$ can stay as a dynamical stable ferromagnetic monolayer crystal. For 1D nanoribbons, it was shown that ARM and ZZ edged structures of the $MnSe_2$ display semiconducting and metallic electronic properties, respectively. Meanwhile, it was predicted that the dimensional reduction leads to structural modifications and therefore FM-to-AFM crossover in the magnetic ground state. When going from 1D to 0D, it was seen that triangular quantum dots of $MnSe_2$ can form various reconstructed edges and all display AFM character in their ground state.

Our calculations reveal that with its highly defect-tolerant crystal structure and size tunable magnetism $MnSe_2$ is a promising material for novel nanoelectronic applications.

Conflicts of interest

There are no conflicts to declare.

Acknowledgements

Computational resources were provided by TUBITAK ULAKBIM, High Performance and Grid Computing Center (TR-Grid e-Infrastructure). HS acknowledges financial support from the TUBITAK under the project number 117F095. HS acknowledges support from Turkish Academy of Sciences under the GEBIP program.

References

1 K. S. Novoselov, A. K. Geim, S. V. Morozov, D. Jiang, Y. Zhang, S. V. Dubonos, I. V. Grigorieva and A. A. Firsov, Electric Field Effect in Atomically Thin Carbon Films, *Science*, 2004, **306**, 666–669.
2 A. K. Geim and K. S. Novoselov, The rise of graphene, *Nat. Mater.*, 2007, **6**, 11–19.

3 A. Nagashima, N. Tejima, Y. Gamou, T. Kawai and C. Oshima, Electronic Structure of Monolayer Hexagonal Boron Nitride Physisorbed on Metal Surfaces, *Phys. Rev. Lett.*, 1995, **75**, 3918.
4 E. Rokuta, Y. Hasegawa, K. Suzuki, Y. Gamou, C. Oshima and A. Nagashima, Phonon Dispersion of an Epitaxial Monolayer Film of Hexagonal Boron Nitride on Ni(111), *Phys. Rev. Lett.*, 1997, **79**, 4609.
5 C. E. Ekuma, V. Dobrosavljević and D. Gunlycke, First-Principles-Based Method for Electron Localization: Application to Monolayer Hexagonal Boron Nitride, *Phys. Rev. Lett.*, 2017, **118**, 106404.
6 P. Vogt, P. De Padova, C. Quaresima, J. Avila, E. Frantzeskakis, M. C. Asensio, A. Resta, B. Ealet and G. Le Lay, Silicene: Compelling Experimental Evidence for Graphenelike Two-Dimensional Silicon, *Phys. Rev. Lett.*, 2012, **108**, 155501.
7 B. Lalmi, H. Oughaddou, H. Enriquez, A. Kara, S. Vizzini, B. Ealet and B. Aufray, Epitaxial growth of a silicene sheet, *Appl. Phys. Lett.*, 2010, **97**, 223109.
8 N. D. Drummond, V. Zólyomi and V. I. Fal'ko, Electrically tunable band gap in silicene, *Phys. Rev. B: Condens. Matter Mater. Phys.*, 2012, **85**, 075423.
9 A. J. Mannix, X.-F. Zhou, B. Kiraly, J. D. Wood, D. Alducin, B. D. Myers, X. Liu, B. L. Fisher, U. Santiago, J. R. Guest, M. J. Yacaman, A. Ponce, A. R. Oganov, M. C. Hersam and N. P. Guisinger, Synthesis of borophenes: Anisotropic, two-dimensional boron polymorphs, *Science*, 2015, **350**, 1513–1516.
10 B. Feng, J. Zhang, Q. Zhong, W. Li, S. Li, H. Li, P. Cheng, S. Meng, L. Chen and K. Wu, Experimental realization of two-dimensional boron sheets, *Nat. Chem.*, 2016, **8**, 563.
11 H. R. Jiang, Z. Lu, M. C. Wu, F. Ciucci and T. S. Zhao, Borophene: A promising anode material offering high specific capacity and high rate capability for lithium-ion batteries, *Nano Energy*, 2016, **23**, 97–104.
12 L. Li, Y. Yu, G. J. Ye, Q. Ge, X. Ou, H. Wu, D. Feng, X. H. Chen and Y. Zhang, Black phosphorus field-effect transistors, *Nat. Nanotechnol.*, 2014, **9**, 372–377.
13 F. Xia, H. Wang and Y. Jia, Rediscovering black phosphorus as an anisotropic layered material for optoelectronics and electronics, *Nat. Commun.*, 2014, **5**, 4458.
14 A. S. Rodin, A. Carvalho and A. H. C. Neto, Strain-induced gap modification in black phosphorus, *Phys. Rev. Lett.*, 2014, **112**, 176801.
15 D. Christiansen, M. Selig, G. Berghäuser, R. Schmidt, I. Niehues, R. Schneider, A. Arora, S. M. de Vasconcellos, R. Bratschitsch, E. Malic and A. Knor, Phonon sidebands in monolayer transition metal dichalcogenides, *Phys. Rev. Lett.*, 2017, **119**, 187402.
16 B. Yang, M. Lohmann, D. Barroso, I. Liao, Z. Lin, Y. Liu, L. Bartels, K. Watanabe, T. Taniguchi and J. Shi, Strong electron-hole symmetric Rashba spin-orbit coupling in graphene/monolayer transition metal dichalcogenide heterostructures, *Phys. Rev. B: Condens. Matter Mater. Phys.*, 2017, **96**, 041409.
17 H.-P. Komsa and A. V. Krasheninnikov, Electronic structures and optical properties of realistic transition metal dichalcogenide heterostructures from first principles, *Phys. Rev. B: Condens. Matter Mater. Phys.*, 2013, **88**, 085318.
18 K. Kośmider, J. W. González and J. Fernández-Rossier, Large spin splitting in the conduction band of transition metal dichalcogenide monolayers, *Phys. Rev. B: Condens. Matter Mater. Phys.*, 2013, **88**, 245436.
19 R.-L. Chu, G.-B. Liu, W. Yao, X. Xu, D. Xiao and C. Zhang, Spin-orbit-coupled quantum wires and Majorana fermions on zigzag edges of monolayer transition-metal dichalcogenides, *Phys. Rev. B: Condens. Matter Mater. Phys.*, 2014, **89**, 155317.
20 Y. T. Hsu, A. Vaezi, M. H. Fischer and E. A. Kim, Topological superconductivity in monolayer transition metal dichalcogenides, *Nat. Commun.*, 2017, **8**, 14985.
21 M. Yagmurcukardes, R. T. Senger, F. M. Peeters and H. Sahin, Mechanical properties of monolayer GaS and GaSe crystals, *Phys. Rev. B*, 2016, **94**, 245407.
22 Q. H. Wang, K. Kalantar-Zadeh, A. Kis, J. N. Coleman and M. S. Strano, Electronics and optoelectronics of two-dimensional transition metal dichalcogenides, *Nat. Nanotechnol.*, 2012, **7**, 699–712.
23 C.-H. Lee, E. C. Silva, L. Calderin, M. A. T. Nguyen, M. J. Hollander, B. Bersch, T. E. Mallouk and J. A. Robinson, Tungsten Ditelluride: a layered semimetal, *Sci. Rep.*, 2015, **5**, 10013.
24 K. F. Mak, C. Lee, J. Hone, J. Shan and T. F. Heinz, Atomically Thin MoS_2: A New Direct-Gap Semiconductor, *Phys. Rev. Lett.*, 2010, **105**, 136805.
25 A. Splendiani, L. Sun, Y. Zhang, T. Li, J. Kim, C.-Y. Chim, G. Galli and F. Wang, Emerging Photoluminescence in Monolayer MoS_2, *Nano Lett.*, 2010, **10**, 1271–1275.
26 Y. Zhang, T. R. Chang, B. Zhou, Y. T. Cui, H. Yan, Z. Liu, F. Schmitt, J. Lee, R. Moore, Y. Chen, H. Lin, H. T. Jeng, S. K. Mo, Z. Hussain, A. Bansil and Z. X. Shen, Direct observation of the transition from indirect to direct bandgap in atomically thin epitaxial $MoSe_2$, *Nat. Nanotechnol.*, 2014, **9**, 111–115.
27 W. Zhao, Z. Ghorannevis, L. Chu, M. Toh, C. Kloc, P.-H. Tan and G. Eda, Evolution of Electronic Structure in Atomically Thin Sheets of WS_2 and WSe_2, *ACS Nano*, 2013, **7**, 791–797.
28 B. Radisavljevic, A. Radenovic, J. Brivio, V. Giacometti and A. Kis, Single-layer MoS_2 transistors, *Nat. Nanotechnol.*, 2012, **6**, 147–150.
29 P. Tonndorf, R. Schmidt, P. Böttger, X. Zhang, J. Börner, A. Liebig, M. Albrecht, C. Kloc, O. Gordan, D. R. Zahn, S. M. de Vasconcellos and R. Bratschitsch, Photoluminescence emission and Raman response of monolayer MoS_2, $MoSe_2$, and WSe_2, *Opt. Express*, 2013, **21**, 4908–4916.
30 O. Kahn and C. J. Martinez, Spin-Transition Polymers: From Molecular Materials Toward Memory Devices, *Science*, 1998, **279**, 44–48.
31 I. Koh and L. Josephson, Magnetic Nanoparticle Sensors, *Sensors*, 2009, **9**, 8130–8145.
32 M. A. McGuire, H. Dixit, V. R. Cooper and B. C. Sales, Coupling of Crystal Structure and Magnetism in the Layered, Ferromagnetic Insulator CrI_3, *Chem. Mater.*, 2014, **27**, 612–620.
33 J. L. Lado and J. Fernández-Rossier, On the origin of magnetic anisotropy in two dimensional CrI_3, *2D Mater.*, 2017, **4**, 035002.

34 F. Iyikanat, M. Yagmurcukardes, R. T. Senger and H. Sahin, Tuning electronic and magnetic properties of monolayer α-$RuCl_3$ by in-plane strain, *J. Mater. Chem. C*, 2018, **6**, 2019–2025.

35 E. Vatansever, S. Sarikurt, F. Ersan, Y. Kadioglu, O. Ü. Aktürk, Y. Yüksel, C. Ataca, E. Aktürk and Ü. Aknc, Strain effects on electronic and magnetic properties of the monolayer α-$RuCl_3$: A first-principles and Monte Carlo study, *J. Appl. Phys.*, 2019, **125**, 083903.

36 B. Huang, G. Clark, E. Navarro-Moratalla, D. R. Klein, R. Cheng, K. L. Seyler, D. Zhong, E. Schmidgall, M. A. McGuire, D. H. Cobden, W. Yao, D. Xiao, P. Jarillo-Herrero and X. Xu, Layer-dependent ferromagnetism in a van der Waals crystal down to the monolayer limit, *Nature*, 2017, **546**, 270–273.

37 C. Gong, L. Li, Z. Li, H. Ji, A. Stern, Y. Xia, T. Cao, W. Bao, C. Wang, Y. Wang, Z. Q. Qiu, R. J. Cava, S. G. Louie, J. Xia and X. Zhang, Discovery of intrinsic ferromagnetism in two-dimensional van der Waals crystals, *Nature*, 2017, **546**, 265–269.

38 E. Torun, H. Sahin, S. K. Singh and F. M. Peeters, Stable half-metallic monolayers of $FeCl_2$, *Appl. Phys. Lett.*, 2015, **106**, 192404.

39 M. Bonilla, S. Kolekar, Y. Ma, H. C. Diaz, V. Kalappattil, R. Das, T. Eggers, H. R. Gutierrez, M.-H. Phan and M. Batzill, Strong room-temperature ferromagnetism in VSe_2 monolayers on van der Waals substrates, *Nat. Nanotechnol.*, 2018, **4**, 289–293.

40 D. J. O'Hara, T. Zhu, A. H. Trout, A. S. Ahmed, Y. K. Luo, C. H. Lee, M. R. Brenner, S. Rajan, J. A. Gupta, D. W. McComb and R. K. Kawakami, Room Temperature Intrinsic Ferromagnetism in Epitaxial Manganese Selenide Films in the Monolayer Limit, *Nano Lett.*, 2018, **18**, 3125–3131.

41 P. Blöchl, Projector augmented-wave method. Efficient iterative schemes for *ab initio* total-energy calculations using a plane-wave basis set, *Phys. Rev. B: Condens. Matter Mater. Phys.*, 1994, **50**, 17953.

42 G. Kresse and J. Hafner, *Ab initio* molecular dynamics for liquid metals. Generalized Gradient Approximation Made Simple, *Phys. Rev. B: Condens. Matter Mater. Phys.*, 1993, **47**, 558.

43 G. Kresse and J. Furthmüller, Efficient iterative schemes for ab initio total-energy calculations using a plane-wave basis set, *Phys. Rev. B: Condens. Matter Mater. Phys.*, 1996, **54**, 11169.

44 J. P. Perdew, K. Burke and M. Ernzerhof, Generalized Gradient Approximation Made Simple, *Phys. Rev. Lett.*, 1996, **77**, 3865.

45 S. L. Dudarev, G. A. Botton, S. Y. Savrasov, C. J. Humphreys and A. P. Sutton, Electron-energy-loss spectra and the structural stability of nickel oxide: An LSDA + U study, *Phys. Rev. B: Condens. Matter Mater. Phys.*, 1998, **57**, 1505.

46 A. Jain, G. Hautier, S. P. Ong, C. J. Moore, C. C. Fischer, K. A. Persson and G. Ceder, Formation enthalpies by mixing GGA and GGA + U calculations, *Phys. Rev. B: Condens. Matter Mater. Phys.*, 2011, **84**, 045115.

47 S. Grimme, Semiempirical GGA-type density functional constructed with a long-range dispersion correction, *J. Comput. Chem.*, 2006, **27**, 1787–1799.

48 A. Togo, F. Oba and I. Tanaka, First-principles calculations of the ferroelastic transition between rutile-type and $CaCl_2$-type SiO_2 at high pressures, *Phys. Rev. B: Condens. Matter Mater. Phys.*, 2008, **78**, 134106.

49 G. Henkelman, A. Arnaldsson and H. Jónsson, A fast and robust algorithm for Bader decomposition of charge density, *Comput. Mater. Sci.*, 2006, **36**, 354–360.

50 M. Kan, S. Adhikari and Q. Sun, Ferromagnetism in MnX_2 (X = S, Se) monolayers, *Phys. Chem. Chem. Phys.*, 2014, **16**, 4990.

51 C. Ataca, H. Sahin and S. Ciraci, Stable, Single-Layer MX_2 Transition-Metal Oxides and Dichalcogenides in a Honeycomb-Like Structure, *J. Phys. Chem. C*, 2012, **116**, 8983–8999.

52 S. Haastrup, M. Strange, M. Pandey, T. Deilmann, P. S. Schmidt, N. F. Hinsche, M. N. Gjerding, D. Torelli, P. M. Larsen, A. C. Riis-Jensen, J. Gath, K. W. Jacosen, J. J. Mortensen, T. Olsen and K. S. Thygesen, The Computational 2D Materials Database: high-throughput modeling and discovery of atomically thin crystals, *2D Mater.*, 2018, **5**, 042002.

53 F. Tran, D. Koller and P. Blaha, Application of screened hybrid functionals to the bulk transition metals Rh, Pd, and Pt, *Phys. Rev. B: Condens. Matter Mater. Phys.*, 2012, **86**, 134406.

54 W. Gao, T. A. Abtew, T. Cai, Y.-Y. Sun, S. Zhang and P. Zhang, On the applicability of hybrid functionals for predicting fundamental properties of metals, *Solid State Commun.*, 2016, **10**, 234.

55 Y.-R. Jang and B. D. Yu, Hybrid Functional Study of the Structural and Electronic Properties of Co and Ni, *J. Phys. Soc. Jpn.*, 2012, **81**, 114715.

56 A. Kuc, N. Zibouche and T. Heine, Influence of quantum confinement on the electronic structure of the transition metal sulfide TS_2, *Phys. Rev. B: Condens. Matter Mater. Phys.*, 2011, **83**, 245213.

57 K. C. Santosh, R. C. Longo, R. Addou, R. M. Wallace and K. Cho, Impact of intrinsic atomic defects on the electronic structure of MoS_2 monolayers, *Nanotechnology*, 2014, **25**, 375703.

58 W. Zhou, X. Zou, S. Najmaei, Z. Liu, Y. Shi, J. Kong, J. Lou, P. M. Ajayan, B. I. Yakobson and J.-C. Idrobo, Intrinsic Structural Defects in Monolayer Molybdenum Disulfide, *Nano Lett.*, 2013, **13**, 2615–2622.

59 X. Li, X. Wang, L. Zhang, S. Lee and H. Dai, Chemically Derived, Ultrasmooth Graphene Nanoribbon Semiconductors, *Science*, 2008, **319**, 1229–1232.

60 J. Cai, P. Ruffieux, R. Jaafar, M. Bieri, T. Braun, S. Blankenburg, M. Muoth, A. P. Seitsonen, M. Saleh, X. Feng, K. Müllen and R. Fasel, Atomically precise bottom-up fabrication of graphene nanoribbons, *Nature*, 2010, **466**, 470–473.

61 Q. Li, J. T. Newberg, E. C. Walter, J. C. Hemminger and R. M. Penner, Polycrystalline Molybdenum Disulfide (2H-MoS_2) Nano- and Microribbons by Electrochemical/Chemical Synthesis, *Nano Lett.*, 2004, **4**, 277–281.

62 Q. Ji, Y. Zhang, T. Gao, Y. Zhang, D. Ma, M. Liu, Y. Chen, X. Qiao, P.-H. Tan, M. Kan, J. Feng, Q. Sun and Z. Liu, Epitaxial Monolayer MoS_2 on Mica with Novel Photoluminescence, *Nano Lett.*, 2013, **13**, 3870–3877.

63 Y. Zhang, Y. Zhang, Q. Ji, J. Ju, H. Yuan, J. Shi, T. Gao, D. Ma, M. Liu, Y. Chen, X. Song, H. Y. Hwang, Y. Cui and Z. Liu, Controlled Growth of High-Quality Monolayer WS_2 Layers on Sapphire and Imaging Its Grain Boundary, *ACS Nano*, 2013, **7**, 8963–8971.

64 J. V. Lauritsen, J. Kibsgaard, S. Helveg, H. Topsøe, B. S. Clausen, E. Lægsgaard and F. Besenbacher, Size-dependent structure of MoS_2 nanocrystals, *Nat. Nanotechnol.*, 2007, **2**, 53.

65 S. Tongay, H. Sahin, C. Ko, A. Luce, W. Fan, K. Liu, J. Zhou, Y.-S. Huang, C.-H. Ho, J. Yan, D. F. Ogletree, S. Aloni, J. Ji, S. Li, J. Li, F. M. Peeters and J. Wu, Monolayer behaviour in bulk ReS_2 due to electronic and vibrational decoupling, *Nat. Commun.*, 2014, **5**, 3252.

66 D. H. Keum, S. Cho, J. H. Kim, D.-H. Choe, H.-J. Sung, M. Kan, H. Kang, J.-Y. Hwang, S. W. Kim, H. Yang, K. J. Chang and Y. H. Lee, Bandgap opening in few-layered monoclinic $MoTe_2$, *Nat. Phys.*, 2015, **11**, 482–486.

67 K.-A. N. Duerloo, Y. Li and E. J. Reed, Structural phase transitions in two-dimensional Mo- and W-dichalcogenide monolayers, *Nat. Commun.*, 2014, **5**, 4214.